Vibrational Control of Covalency Effects Related to the Active Sites of Molybdenum Enzymes

Benjamin W. Stein[1,2], Jing Yang[1], Regina Mtei[1], Nicholas J. Wiebelhaus[3], Dominic K. Kersi[1], Jesse LePluart[1], Dennis L. Lichtenberger[3], John H. Enemark[3]*, Martin L. Kirk[1]*.

[1]Department of Chemistry and Chemical Biology, The University of New Mexico, MSC 032060, 1 University of New Mexico, Albuquerque, New Mexico 87131, United States.

[2]Chemistry Division, Los Alamos National Laboratory, Los Alamos, New Mexico, 87545, United States.

[3]Department of Chemistry and Biochemistry, The University of Arizona, 1306 E. University Blvd., Tucson, Arizona 85721, United States.

mkirk@unm.edu

jenemark@email.arizona.edu

KEYWORDS (Word Style "BG_Keywords"). If you are submitting your paper to a journal that requires keywords, provide significant keywords to aid the reader in literature retrieval.

ABSTRACT: A multi-technique spectroscopic and theoretical study of the Cp_2M(benzenedithiolato) (M=Ti,V,Mo; Cp = η^5-C_5H_5) series provides deep insight into dithiolene electronic structure contributions to electron transfer reactivity and reduction potential modulation in pyranopterin molybdenum enzymes. This work explains the magnitude of the dithiolene folding distortion, and the concomitant changes in metal-ligand covalency, that are sensitive to electronic structure changes as a function of d-electron occupancy in the redox orbital. It is shown that the large fold angle differences correlate with covalency, and the fold angle distortion is due to a pseudo-Jahn-Teller (PJT) effect. The PJT effect in these and related transition metal dithiolene systems arise from the small energy differences between metal and sulfur valence molecular orbitals, which uniquely poise these systems for dramatic geometric and electronic structure changes as the oxidation state changes. Herein, we have used a combination of resonance Raman, magnetic circular dichroism, electron paramagnetic resonance, and UV photoelectron spectroscopies to explore the electronic states involved in the vibronic coupling mechanism. Comparison between the UV photoelectron spectroscopy (UPS) of the d^2 M=Mo complex and the resonance Raman spectra of the d^1 M=V complex reveals the power of this combined spectroscopic approach. Here, we observe that the UPS spectrum of Cp_2Mo(bdt) contains an intriguing vibronic progession that is dominated by a "missing-mode" that is comprised of PJT active distortions. We discuss the relationship of the PJT distortions to facile electron transfer in molybdenum enzymes.

Introduction

In the 1960s[2] it was shown that metallodithiolene complexes with redox active metals possess unusual electronic structures when combined with the inherent redox activity of the dithiolene ligand. This non-innocent property has propelled a resurgent interest[3-4] in using metallodithiolenes in industrial applications,[5-7] as catalysts,[8] and for their interesting photophysical properties.[9] Additionally, the discovery of the dithiolene chelate as a critical component of the pyranopterin cofactor (Figure), which is found in all mononuclear Mo and W enzymes,[10] has driven new questions regarding why Nature has selected dithiolenes over other sulfur donors (e.g. cysteine) in order to facilitate a wide variety of enzyme catalyzed reactions using second and third row transition metals. Dithiolene ligands are well-known to stabilize transition metal centers in multiple oxidation states, a requirement for performing oxidative and reductive oxygen two-electron atom transfer reactions.[4] While the specific function of the pyranopterin dithiolene in the catalytic cycles of molybdoenzymes has yet to be determined,[11] the "non-innocent character" of dithiolene ligands is likely to be a key contributor to catalysis at the active site. Thus, correlating electronic structure with the nature of potential energy surfaces (PES) and the dynamics of the metal-dithiolene interaction is of vital importance to advancing understanding of this ligand in metalloenzyme catalysis.

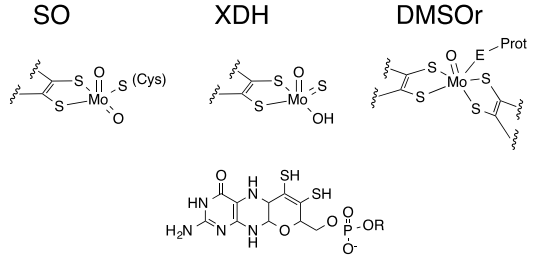

Figure 1: Accepted structures for the active sites of the three canonical Mo enzyme families (top) and the reduced form of the pyranopterin dithiolene cofactor (bottom). R = H or dinucleotide. SO: sulfite oxidase family; XDH: xanthine dehydrogenase family; DMSOr: dimethyl sulfoxide reductase family.

X-ray crystal structures of molybdoenzymes exhibit a range of molybdenum-dithiolene fold angles (defined as the angle between a plane formed by the metal and two sulfur atoms and one formed by the two sulfurs and the dithiolene carbons).[12-16] However, obtaining crystal structures of proteins with sufficiently high resolution to make precise geometric measurements is formidable, and the active sites often undergo auto-reduction under X-ray radiation,[17] making it difficult to correlate oxidation state to dithio-

lene-metal geometry. Furthermore, direct spectral probing of the pyranopterin dithiolene in molybdoenzymes has proven to be difficult. Thus, model compounds are used to help understand the metal-dithiolene interaction and how this interaction may be manifest in the active sites of molybdoenzymes. A convenient platform for these studies has been molecules of the type $Cp_2M(bdt)$ (M = Ti, V, Mo; bdt = benzenedithiolato; Cp = η^5-C_5H_5) due to the fact that they have been characterized by x-ray crystallography and their d-electron counts (d^0, d^1, d^2), are directly relevant to those found in the Mo(VI), Mo(V), and Mo(IV) enzyme forms, respectively.[18-19] Thus, this series of $Cp_2M(bdt)$ compounds allows for a direct probe of the nature of the metal-dithiolene interaction as a function of d-electron count and *at parity of the dithiolene and ancillary ligands*. This critical comparison has not been possible with other model systems.[13]

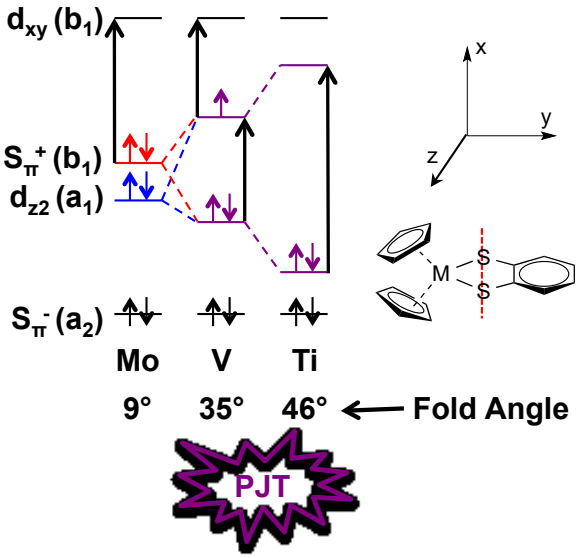

Figure 2: Frontier molecular orbital diagram for $Cp_2M(bdt)$, (M=Mo,V,Ti). Arrows indicate band assignments of dominant absorption features as discussed in text. S_{π}^{+} and S_{π}^{-} refer to the in-phase and out-of-phase sulfur p orbital combinations, respectively. Orbital notation follows that given previously in the literature[1]. The molybdenum-dithiolene fold is along the S-S vector (red dashed line). The pseudo Jahn-Teller (PJT) effect is important in the V and Ti compounds. Red line: ligand-based orbital; Blue line: metal-based orbital; Purple line: strongly mixed metal + ligand orbitals.

Initial links between the electronic and molecular structure of bent metallocene-dithiolene compounds were first posited by Lauher and Hoffman in 1975,[18] who related the "folding" within the metal-dithiolene chelate ring to the d-electron configuration of the metal. This metal-dithiolene folding along the ligand S-S vector brings a filled symmetric $S_{p\pi}$ orbital (hereafter referred to as $S_{\pi+}$) into direct overlap with an in-plane metal orbital of the same symmetry. This orbital overlap allows the ligand to donate electron density to an unoccupied or singly occupied in-plane metal d orbital. The folding has a pronounced effect on the frontier molecular orbital structure of these compounds (Figure 2).[2, 20] This "ligand folding" effect becomes more prominent as the d-electron count decreases (d^2 = 9°,

d^1 = 35°, d^0 = 46°),[19] and allows for the holes created by lost electrons to be delocalized in metal-dithiolene orbitals.[19, 21] These studies have formed the basis for a hypothesis asserting that the pyranopterin dithiolene ligand may be an active participant in the catalytic cycles of Mo/W enzymes by modulating active site redox potentials through static or dynamic changes in metal-dithiolene covalency.[22-23] For example, in the proposed catalytic cycle of sulfite oxidase the Mo center traverses through three different formal oxidation states during two sequential one-electron oxidations of the Mo(IV) species back to the active Mo(VI) form. Recently, it was suggested that coupling the intermediate Mo(V) (d^1) form with fold angle variation at the sulfur atoms of the pyranopterin dithiolene ligand can provide a lower energy reaction pathway for these sequential one-electron reoxidation steps of the catalytic pathway. **1**

In an effort to develop a more comprehensive understanding of how electron configuration affects metallodithiolene electronic and geometric structure in archetypical $Cp_2M(bdt)$ complexes, we have performed a combination of electronic absorption, resonance Raman (rR), magnetic circular dichroism (MCD), and gas-phase UV photoelectron spectroscopies (UPS). These spectroscopic studies are complemented by electronic structure calculations in order to assign low-energy optical and vibrational transitions that provide deep insight into the vibronic origins of ligand folding as a function of electron configuration, and develop a greater understanding of the role of the pyranopterin dithiolene in molybdoenzymes. Specifically, we show that the ligand folding distortions result from a pseudo Jahn-Teller (PJT) effect, which arises from the vibronic coupling of the ground electronic state with an excited electronic state, and enables symmetry-forbidden mixing of states via a configuration interaction mechanism in order to control metal-ligand covalency.

Experimental

Synthesis. Starting materials, Cp_2MoCl_2 (Alfa Aesar), Cp_2VCl_2, Cp_2TiCl_2 (Aldrich) and 1,2-benzenedithiol (Aldrich) were purchased and used without further purification. Synthesis of the compounds $Cp_2M(bdt)$ (M= Mo, Ti, V) was carried out as previously described in the literature[24-26] using

standard Schlenk techniques. Identification of the compounds was aided by electronic absorption spectroscopy and mass spectrometry.

Photoelectron spectroscopy (UPS). The gas-phase UPS spectrum of $Cp_2Mo(bdt)$ was collected using the instrument and procedures that have been described previously.[27] The instrumentation is interfaced via a National Instruments PCIe-6259 multi-function data acquisition card with customized software. Resolution measured during data collection (taken as the fwhm of the Ar $^2P_{3/2}$) was 0.025-0.030 eV. The sublimation temperature of the sample (measured at 10^{-5} Torr and using a "K" type thermocouple attached to an aluminum sample cell) was 190-200˚C. The sample showed no signs of decomposition during collection.

Electronic Absorption Spectroscopy. Solution electronic absorption spectra were collected using a double beam Hitachi U-3501 UV-Vis-NIR spectrophotometer capable of scanning a wavelength region between 185 and 3200 nm. All absorption spectra were collected at 2.0 nm slit width in the UV-visible range and with a variable slit width in the NIR. The instrument was calibrated with reference to the 656.10 nm deuterium line. Solution samples were prepared by dissolving the compounds in degassed dichloromethane (M=Mo,Ti) or 2-methyltetrahydrofuran (M=V). The electronic absorption spectra were subsequently collected in 1 cm pathlength quartz cells (blackmasked Suprasil, equipped with a Teflon lined screw cap). Gaussian resolution of spectral bands was accomplished with the Magicplot software package (Magicplot systems, LLC).

Magnetic Circular Dichroism Spectroscopy. Low-temperature MCD data were collected on a system consisting of a Jasco J810 CD spectropolarimeter employing Hamamatsu photomultiplier tubes of either S-1 or S-20 response, an Oxford Instruments SM4000-7T superconducting magneto-optical cryostat (0-7 Tesla and 1.4-300 K), and an Oxford Instruments ITC503 temperature controller. The spectrometer was calibrated for CD intensity and wavelength using camphorsulfonic acid and a Nd-doped reference glass sample (Schott Glass). MCD samples were prepared as frozen 2-methyltetrahydrofuran (Alfa Ae-

sar, purified by passage down a column of activated alumina followed by immediate freeze-pump-thaw degassing) solutions. The sample cell was loaded under an N_2 atmosphere and immediately frozen in liquid N_2 due to the observed O_2 sensitivity of $Cp_2V(bdt)$ in solution. Depolarization of the incident radiation was checked by comparing the difference in CD intensity of a standard Ni (+)-tartrate solution positioned before and then after the sample. Samples which depolarized the light by <5% were deemed suitable. All MCD spectra were collected in an applied magnetic field of 7T, and a 0T spectrum was subtracted to correct for field-independent effects.

Resonance Raman Spectroscopy. Resonance Raman spectra were collected in a 180° (780 nm) or 90° (all other lines) geometry. Coherent Innova 70C (5W) Ar^+ and 300C Kr^+ ion lasers were used as the photon sources. The scattered radiation was passed through a longpass filter (Semrock RazorEdge) to remove Rayleigh scatter laser light and then dispersed onto a liquid N_2 cooled 1" Infrared Associates CCD detector using a Princeton Acton spectrograph. The laser power at the sample was kept between 40 and 100 mW in order to prevent possible photo- and thermal degradation of the sample. 780 nm Raman spectra were collected with a Thermo-Scientific DXR SmartRaman, using a low 2 mW laser power due to the observed sensitivity of $Cp_2V(bdt)$ to photodegradation. Solid samples were prepared as finely ground powders and dispersed in a NaCl(s) matrix with Na_2SO_4 added as an internal standard. These samples were subsequently either sealed in a glass capillary tube and spun with a custom made sample holder or thinly spread on carbon tape and held in a standard brass holder (780 nm). The construction of resonance Raman profiles was accomplished by comparing the integrated intensity of a Raman band at a given excitation wavelength relative to that of the 992.4 cm^{-1} band of Na_2SO_4 or solvent bands. All data were scan-averaged, and any individual data set with vibrational bands compromised by cosmic events was discarded.

Electron Paramagnetic Resonance Spectroscopy. The room temperature (300K) solution EPR spectrum of $Cp_2V(bdt)$ was collected at X-band (9.388186 GHz;) using a Bruker EMX spectrometer with

associated Bruker magnet control electronics and microwave bridges. A microwave power of 20 dB was used for all experiments. Simulations of the EPR spectra were performed using the MATLAB toolbox EasySpin,[28] with further analyses performed using in-house written scripts for the program Visual Molecular Dynamics.[29]

Computations. Resonance Raman calculations and spectral fitting were performed with the Advanced Spectral Analysis (ASA) package of ORCA 3.0.0.[30-33] Resonance Raman spectra were calculated by setting the theoretical excitation energy to be equal to the TDDFT calculated transition energy. Individual one-electron promotion contributions to the TDDFT transition were considered independently when computing the Raman spectrum under resonance conditions. This was done to understand which one-electron configuration was dominantly responsible for the calculated resonance Raman enhancement pattern. Geometry optimizations and frequency calculations used the def2-TZVPP[34] basis set and the PBE[35] functional, while TD-DFT spectra and the excited state gradients[36] used in the calculation of resonance Raman spectra were calculated with the PBE0 hybrid functional[37-38] and the RIJCOSX approximation[39]. TD-DFT calculations of MCD spectra were done with ADF 2012.01[40-41] using a triple-ζ STO basis (TZP) and the PBE functional (this version of ADF does not support MCD calculations with hybrid functionals, however, transitions were carefully analyzed to ensure agreement between hybrid and GGA functionals). Electron density difference maps (EDDMs) were created using the *orca_plot* utility within the ORCA suite. All orbital and EDDM figures were created with VMD.[29] For d^1 **2**, orbitals were visualized as quasi-restricted orbitals (QROs).[42]

Results and Discussion

Here we present an analysis of spectroscopic data for the tetravalent metal series $Cp_2Mo(bdt)$ (**1**), $Cp_2V(bdt)$ (**2**), and $Cp_2Ti(bdt)$ (**3**), which are interpreted in the context of detailed bonding and spectroscopic calculations. A simple four orbital model (Figure 2) is used in the analysis of the data to develop a pseudo-Jahn-Teller (PJT) description of ligand folding in metallodithiolenes, and to understand how

the interplay between electronic and geometric structure uniquely poises the d^1 configuration for tunable facile electron transfer processes like those observed in the Mo(V) state of pyranopterin molybdenum enzymes. The results and analysis of **1**-**3** will each be discussed in turn, and we begin with closed shell **1**, which can be effectively used as a foundation for understanding the electronic structures of **2** and **3**.

<u>$Cp_2Mo(bdt)$</u>

Electronic Structure and Spectroscopy of $Cp_2Mo(bdt)$, The frontier molecular orbitals of **1** are presented in Figure 3 and are similar to those computed previously for this molecule.[20] and symmetry labels are provided assuming an idealized C_{2v} geometry. The a_1 HOMO-1 orbital is primarily metal-based, and in our coordinate frame this is the Mo d_{z2} orbital. The b_1 HOMO is a dithiolene orbital (S_π^+) and does not effectively mix with the b_1 LUMO (Mo d_{xy} + Cp_2) due to the large computed energy gap between these two orbitals (~ 3.6 eV). Additionally, the HOMO and HOMO-1 are orthogonal and therefore cannot mix. Inspection of the MO diagram for **1** suggests the presence of two low-energy excitations. The first is a low-energy ligand-to-metal charge transfer (LMCT) transition from the doubly occupied S_π^+ HOMO orbital to the vacant d_{xy}. The second is a formally ligand field (LF) transition described as a one-electron promotion from the doubly occupied d_{z2} orbital to d_{xy}. A complete listing of the TD-DFT computationally assisted band assignments for the higher energy bands is presented in Table S-1.

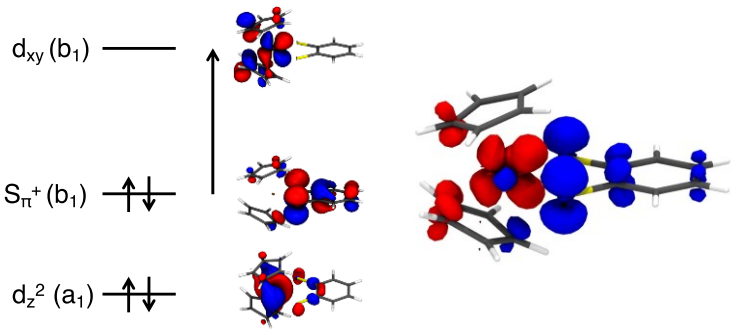

Figure 3: Left: Calculated frontier molecular orbitals of **1**. Arrow denotes calculated low energy LMCT probed by electronic absorption and rR spectroscopies. Right: The electron density difference map (EDDM) for this LMCT transition (blue: electron loss in the transition, red: electron gain in the transition). The computed composition of the EDDM is ~90% $S_\pi^+ \rightarrow d_{xy}$ LMCT in character. Isovalues: 0.04 (orbitals), 0.004 (EDDM).

The solution electronic absorption spectrum, selected resonance Raman (rR) profiles, experimental rR spectrum, and computed rR spectrum for **1** are shown in Figures 4A and 4B. As anticipated from the molecular orbital description, **1** possesses a single absorption feature (Band I) at low-energy (20,614 cm^{-1}) that is energetically isolated from higher energy excitations. The HOMO→LUMO LMCT transition is anticipated to possess a markedly greater oscillator strength than the LF transition, and this allows us to assign Band I as the $S_{\pi}^{+} \rightarrow d_{xy}$ charge transfer transition. We note that the $d_{z2} \rightarrow d_{xy}$ LF transition is likely obscured by the CT absorption envelope, precluding the direct observation of this transition in the electronic absorption spectrum. The computed electron density difference map (Figure 3, right) depicts the electron density redistribution that results from the $S_{\pi}^{+} \rightarrow d_{xy}$ one-electron promotion. The Mo d_{xy} LUMO is strongly antibonding with respect to the two Cp rings and therefore the electron density redistribution that accompanies the $S_{\pi}^{+} \rightarrow d_{xy}$ LMCT transition is expected to result in a large excited state distortion along the totally symmetric Cp-Mo-Cp stretching coordinate leading to rR enhancement of the a_1 Cp-Mo-Cp stretching vibration.

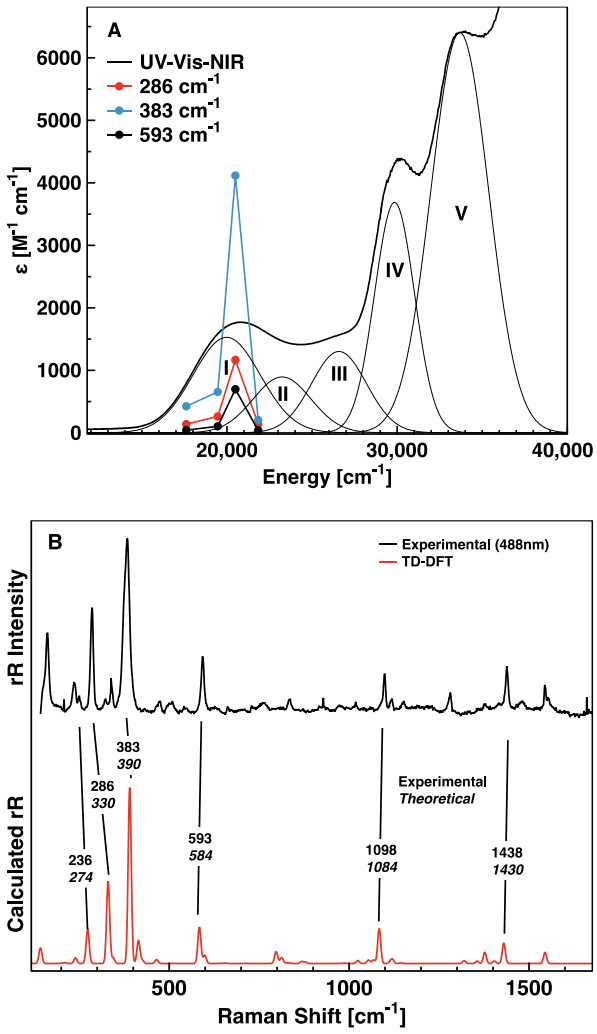

Figure 4A: Solution (CH_2Cl_2) absorption spectrum and resonance Raman profiles of $Cp_2Mo(bdt)$ (**1**). Gaussian resolved bands are denoted with Roman numerals. 4B: Experimental (CH_2Cl_2) and theoretical (PBE0) resonance Raman spectra for **1**. Experimental excitation wavelength: 488 nm (in resonance with band I), theoretical: 444 nm (in resonance with calculated λ_{max}). Numbers in the figure denote the vibrational frequencies (normal font: experimental; italic: theoretical).

Resonance Raman spectroscopy, through the analysis of Raman profiles and relative enhancement of vibrational modes under resonance conditions, provides an extremely powerful probe for identifying the nature of the CT excited state by detailing how the excited state geometry is distorted relative to the

ground state geometry. Here, we have used a combination of experimental and computed Raman spectra, obtained on resonance with Band I, to analyze the relative rR enhancement patterns of the vibrational modes, make detailed assignments of the vibrational spectra, and support our assignment of Band I. The most intense resonance Raman vibration of **1** is the 383 cm^{-1} mode, which is assigned as the totally symmetric Cp-Mo-Cp stretch. This strongly supports the assignment of Band I in the electronic absorption spectrum as the $S_{\pi}^{+} \rightarrow d_{xy}$ LMCT transition with a large excited state distortion along the totally symmetric Cp-Mo-Cp coordinate relative to the ground state. Raman vibrations occurring at 1438 cm^{-1}, 1098 cm^{-1}, 593 cm^{-1}, 286 cm^{-1}, and 236 cm^{-1} also show strong resonance enhancement with excitation into Band I. These modes have been assigned (Table 1) on the basis of their DFT computed frequencies and, most importantly, by their remarkably similar relative resonance enhancements compared with experiment. As such, the agreement between experimental and computed rR spectra provide additional evidence in support of our assignment of Band I as a $S_{\pi}^{+} \rightarrow d_{yz}$ LMCT transition. In addition, the absence of a resonantly enhanced totally symmetric S-Mo-S stretch, further supports the molecular orbital description of minimal S_{π}^{+} - d_{z2} and S_{π}^{+} - d_{xy} orbital mixing, leading to a planar dithiolene chelate ring in the effective ~C_{2v} geometry of **1.** Of crucial importance is the fact that the resonance Raman enhancement is dominated by the occupation of the d_{xy} orbital, which is *not* equivalent to the electron density change that occurs during the photoelectron process, *vide infra,* since photoejection from S_{π}^{+} does not lead to d_{xy} orbital occupation.

Photoelectron spectroscopy (UPS) of $Cp_2Mo(bdt)$. Ultraviolet photoelectron spectroscopy (UPS) is used to probe the energies of molecular orbitals by relating molecular ionization energies to the energy of the orbital from which the photoionized electron originated (Koopmans' theorem). This ionization process may also be viewed as an electronic transition from the ground state of a neutral molecule (e.g. **1**) to a cationic state plus an electron ((e.g. $\mathbf{1}^{+}$, Figure 5). As such, the profile of the ionization band contains valuable information regarding the vibrational structure of the photogenerated cation. If the fre-

quency of the vibration along a distortion coordinate is large enough,[43] the vibrational structure of the cation may be resolved in the photoelectron spectrum, and the observation of vibronic structure can provide a wealth of electronic structure information.[43] For example, the frequency of excited state vibrations can be used to determine how a molecule distorts following photoionization of an electron from a given molecular orbital. One may also determine the reorganization energy, λ, that is associated with the electron loss.[44-45] A particular advantage of determining λ using gas-phase photoelectron spectroscopy is the absence of solvent contributions to the spectrum. Here, we use UPS to gain additional insight into the electronic and vibrational structure of **1** and its cation, $\mathbf{1}^+$.

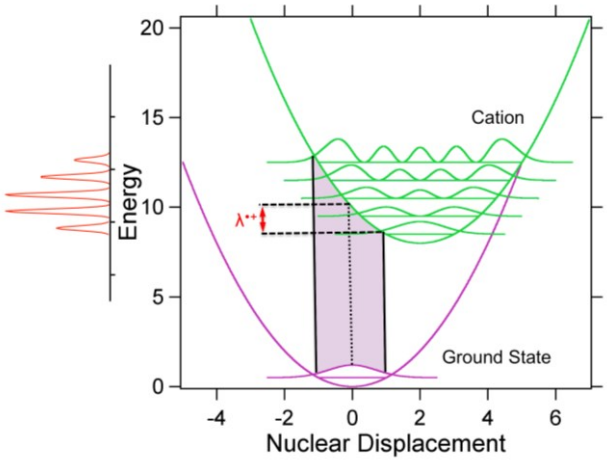

Figure 5: A schematic representation of the ionization process. A single ionization band will be constituted by peaks from individual vibrational levels of the cation (left). The reorganization energy, λ_v, here, is taken as the difference in energy between the vertical ionization energy (dotted line) and the adiabatic ionization energy.

Vibrational structure is clearly resolved in the UPS first ionization band of **1** (Figure 6) that derives from photoemission of an electron from the HOMO, which is predominantly $S_{\pi+}$ in character.[13] Using methods described previously,[46] we have performed a vibrational analysis of the $S_{\pi+}$ first ionization band for **1**. The UPS data can be fit analytically using a vibrational progression with a Poisson distribution of symmetric Gaussians peaks whose intensities (I) are governed by Eqn 1:

$$I_n = \frac{S^n}{n!} e^{-S} \qquad (1)$$

where n indexes the vibrational level and S is the Huang-Rhys factor relating the vertical transition to the vibrational progression.[47] Peak positions were found to be reproducible to ± 0.02 eV. The vertical length of the data points in Figure 6 represents the experimental variance at each data point. The best fit to the data emphasizing the initial vibrational levels on the low ionization energy side of the band yields a vibrational progression frequency, ν, of 0.047 ± 0.008 eV (383 ± 65 cm^{-1}) and an S of 4.07. The re-

duction in intensity on the high energy side of the fit is due to the contribution of lower energy, unresolved vibrations. Deviations between the best fit and the data in the lowest energy region are due to the presence of hot bands generated by the population of excited vibrational levels in the ground electronic state. The reorganization energy, $\lambda = 0.19 \pm 0.04$ eV, can be calculated using Eqn. 2:[47]

$$\lambda = \sum_k S_k h\nu_k \qquad (2)$$

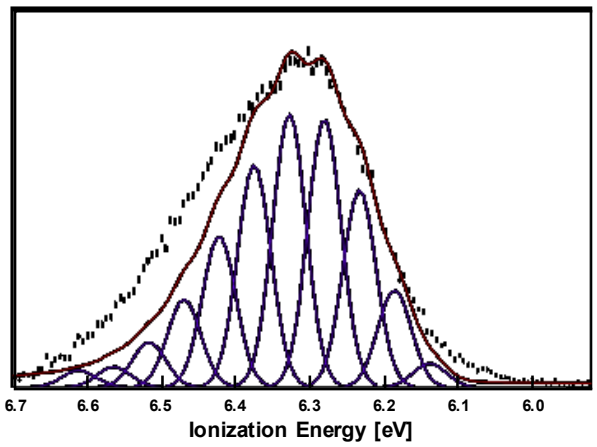

Figure 6: Close-up of the first ionization band of the gas-phase UPS spectrum of $Cp_2Mo(bdt)$ (**1**). Also shown is the fit for vibrational structure with a Poisson distribution. The spacing of the peaks in the Poisson distribution corresponds to the 383 cm^{-1} vibronic progression that is activated by ionization from HOMO of **1**.

where, h is Planck's constant and ν_k is the frequency of the kth vibrational mode. The S and λ_v values are larger than would generally be expected for photoionization of an electron from a non-bonding orbital. The computationally derived reorganization energy, taken to be the ΔSCF value of the geometry optimized cation and the cation in the optimized geometry of the neutral molecule, was found to be 0.19 eV, in full agreement with experiment. These results strongly suggest a significant structural change in $\mathbf{1}^+$ relative to **1**, which results in new covalency contributions to the bonding scheme.[43] The data are consistent with the idea that this new bonding interaction is formed between the S_π^+ orbital and the metal d-orbitals when there is a reduction in the d-electron count from 2 to 1. Orbital mixing between S_π^+ and Mo d_{z2}, leading to new covalency, requires that the symmetry be lowered since S_π^+ and Mo d_{z2} do not transform as the same irreducible representation in the C_{2v} point group.

The 383 cm^{-1} Cp-M-Cp stretch observed by rR is a ground state vibrational mode for the *neutral* species (**1**) and not the *cationic* form ($\mathbf{1}^+$) that is directly probed in the UPS experiment (Figure 5). The rR enhancement of the Cp-M-Cp stretching vibration in **1** that is observed with optical pumping into Band I results from population of the d_{xy} orbital in the LMCT excited state. However, the d_{xy} orbital is not oc-

cupied during the **1** → **1**$^+$ photoemission process that is probed by UPS. As a result, the resonance Raman spectrum of **1** does not fully explain the vibronic structure observed in UPS spectrum of this complex. In order to understand the nature of the excited state distortion that is responsible for the vibronic structure observed in the ionization envelope of the first ionization band resulting from S_π^+ photoemission; geometry optimizations were performed on both **1** and **1**$^+$. Determination of the vibrational modes that contribute to the observed vibrational progression was accomplished by the projection of Cartesian displacement differences between the calculated geometries of the neutral and cationic forms of **1** onto dimensionless normal coordinate (derived from frequency calculations of the cation) displacements.

Although three vibrational modes with computed frequencies near the experimental value possess sizeable displacements relative to the ground state geometry (Table 2), the largest distortion is found along a mode that occurs at a higher frequency (474 cm^{-1}) than the observed 383 cm^{-1} UPS vibronic progression. We note that the appearance of an *effective* observed frequency does not necessarily equate with an actual vibrational mode of the molecule, but can be described as a weighted average of the actual vibrational modes of the complex. This phenomenon has been extensively studied by Heller, and is known as the missing mode effect (MIME).[48] The MIME frequency is described by the following equation for the effective (missing) mode:

$$\omega_{eff} = \frac{\sum_k \omega_k^2 \Delta_k^2 + 4\Gamma^2}{\sum_k \omega_k \Delta_k^2 n_k} \qquad (3)$$

where ω are the vibrational modes, Δ are the dimensionless displacements, n_k corresponds to the number of vibrational periods in which the interacting modes need to return to a position of maximal overlap, and Γ is a broadening factor (typically ~100 cm^{-1}). Equation 3 can be solved iteratively, and the solution of this equation (using *all* modes, not just those in Table) results in an effective frequency (ω_{eff}) of 394 cm^{-1}, which is in excellent agreement with the observed experimental UPS progression frequency of 383 ± 65 cm^{-1}. This strongly supports the use of the MIME methodology for describing the origin of the vibronic progression observed in the UPS spectrum of **1**. The higher energy vibrational contribution

(474 cm^{-1}) primarily consists of dithiolene C-S stretching character, which is expected for the loss of an S_{π}^{+} electron due to photoionization. The lower frequency modes (calculated at 332 cm^{-1} and 311 cm^{-1}), however, have appreciable Mo-Cp stretching character, and this demonstrates the role of electronic relaxation in the ionization process and/or the degree of Cp-bdt antibonding character in the frontier MOs. Upon ionization of an electron from the S_{π}^{+} orbital, a pseudo Jahn-Teller effect is immediately operational (*vide infra*), which mixes the d_{z2} and S_{π}^{+} orbitals. The appreciable degree of Mo-Cp pseudo σ* character that is present in the d_{z2} orbital[20] nicely explains the observed distortion along the Cp-Mo-Cp coordinate.

<u>$Cp_2V(bdt)$</u>

Electronic Structure and Spectroscopy of $Cp_2V(bdt)$. The frontier molecular orbitals of **2** are presented in Figure 7 as quasi-restricted orbitals (QROs) for a more direct comparison with the closed-shell spin-restricted calculations of **1** and **3**. These QROs can be obtained from the natural orbitals that derive from a spin unrestricted Kohn-Sham computation and they possess energies that are well defined.[42] Using this QRO approach, we find that the energies of the d_z^2 and S_π^+ orbitals are reversed relative to those observed for **1**, with the SOMO being primarily d_z^2 based and the HOMO being primarily ligand based S_π^+. The appearance of these QROs and their relative energies are similar to those computed using a spin unrestricted DFT approach.[1] The computed α-orbital in the spin unrestricted calculation (Figure S-8), which is most similar to the SOMO for **2,** shows more mixing between the V d_z^2 QRO SOMO and the S_π^+ HOMO. Using the QRO functions, enhanced covalency is obtained from configurational mixing between the ground configuration (shown in Figure 7) and the excited configuration that derives from a HOMO → SOMO one-electron promotion. This enhanced covalency is qualitatively illustrated in Figure 2 and results in the isotropic EPR g-value being close to the free-ion value of 2.0023. Although **2** possesses a bent C_s idealized geometry, we continue to use the same idealized C_{2v} symmetry labels in order to more easily correlate these orbitals with those of **1**. In the bent geometry of **2**, the d_z^2 SOMO and the S_π^+

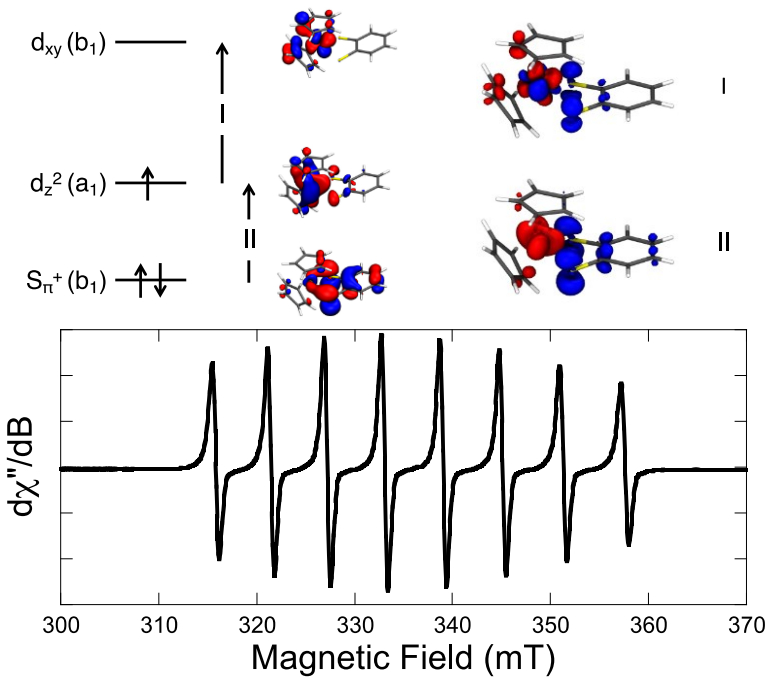

Figure 7: Top: Frontier quasi-restricted MOs (QROs) for **2**. Right: Arrows denote major transitions in the low-energy LMCT region. EDDMs for the transitions are given on the right (blue: electron loss, red: electron gain). Isovalues: 0.04 (orbitals), 0.004 (EDDM). Bottom: RT EPR spectrum of **2** (g_{iso} = 1.9923; A_{iso} (^{51}V) = 166 MHz). Note that the Mo(z^2) – Sπ+ mixing provides a covalency and charge transfer mechanism for g_{iso} ~2.

HOMO possess the same symmetry and can therefore mix, with the degree of this mixing probed by the intensity of the HOMO → SOMO charge transfer transition.[23, 49-50]

The electronic absorption spectrum of **2** (Figure 8A) shows a similar overall absorption envelope as **1**, but with a distinct red shift of the observed bands. Although an apparent low energy tail is observed on the low-energy band, the individual transitions responsible for the spectral bandshape are not resolved in the room temperature absorption spectra. The electronic transitions in **2** are revealed at higher resolution in the low temperature frozen solution MCD spectrum (Figure 8A). Here, the data clearly show that two transitions contribute to the absorption envelope of the lowest energy band. This is of particular significance, since the simple MO model depicted in Figure 2 predicts several possible CT transitions that are likely to occur at similar energies. These include the $S_{\pi}^{+} \rightarrow d_{xy}$ and $S_{\pi}^{+} \rightarrow d_{z2}$ LMCT transitions and the $d_{z2} \rightarrow d_{xy}$ ligand field transition. We assign Band I as the $d_{z2} \rightarrow d_{xy}$ LF transition due to the weaker absorption intensity and relatively large C/D ratio (MCD C-term intensity/dipole strength) which suggests that Band I has dominant LF character.[51] This allows Band II to be assigned as a $S_{\pi}^{+} \rightarrow d_{z2}$ transition due to the markedly smaller C/D ratio and higher extinction coefficient anticipated for a LMCT transition.

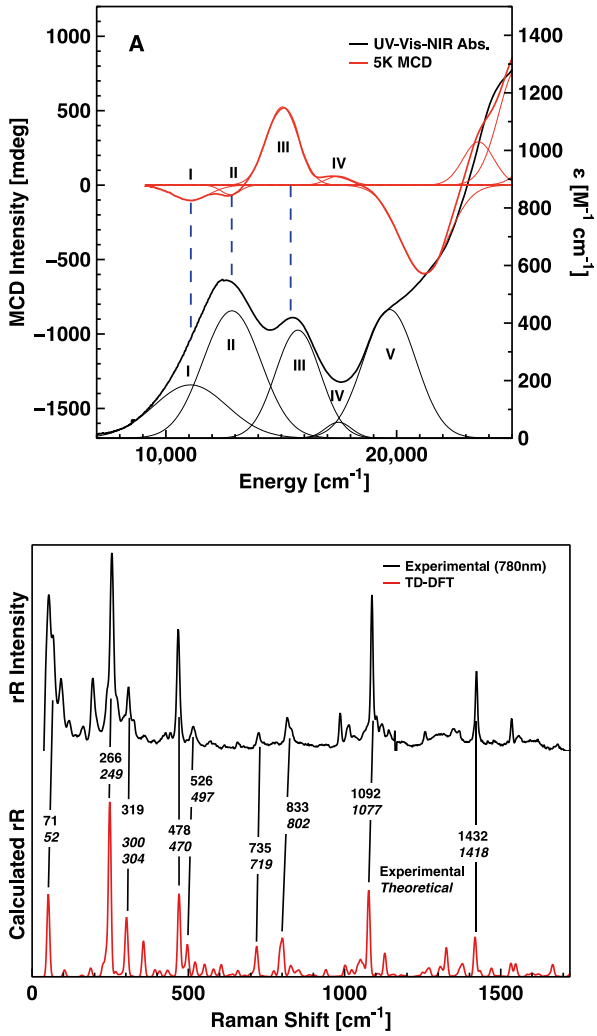

Figure 8. A: Gaussian deconvoluted solution absorption spectrum (RT) and MCD spectra (5K, 7T) of **2** (M=V). Solvent: 2-Me-THF. Gaussian resolved bands are denoted with roman numerals. Dashed lines are a guide to the eye to show the concurrence between transitions in the MCD and UV-Visible-NIR spectra. B: Experimental (solid, NaCl matrix, Na_2SO_4 internal standard) and theoretical (PBE0) resonance Raman spectra for **2**. Experimental excitation wavelength: 780 nm, theoretical: 855 nm (in resonance with calculated λ_{max} of band II).

Although CT transitions that involve a bonding/antibonding pair of orbitals are expected to possess appreciable absorption intensity, the absence of any d-orbital rotation in the $S_{\pi}^{+} \rightarrow d_{z2}$ transition limits spin-orbit coupling contributions to the transition and therefore

there should be little MCD intensity and a corresponding small C/D ratio.[23, 51] Increased mixing of the S_{π}^{+} and d_{z2} orbitals is made possible by the chelate fold angle distortion observed in the crystal structure of **2**. This distortion is driven by the removal of one electron from the metal-based HOMO-1 orbital of **1** (Figure 3), resulting in increased covalency that is directly probed by the intensity of the $S_{\pi}^{+} \rightarrow d_{z2}$ transition. Further support for this assignment is provided by the calculated MCD and electronic absorption spectra of **2**, which can be qualitatively compared with the experimental results at energies $\lessapprox$ 15,000 cm^{-1} (Figure S-1). A complete listing of the TD-DFT computationally assisted band assignments for the higher energy bands is presented in Table S-2.

The low-energy resonance Raman spectrum of **2** (Figure 8B), collected in resonance with bands I and II, shows an increase in the number of resonantly enhanced vibrations when compared to **1**. This suggests either a marked reduction in the symmetry of the molecule (e.g. a large dithiolene chelate fold) and/or a distinct difference in the nature of the electronic transitions that contribute to the low energy absorption band. The former does not appear to substantially affect the resonance Raman enhancement, as a change in geometry does cause a shift in the rR profile maximum (e.g. **1**, see Figure S-2 for an example involving the solid-state spectrum) but not in the enhancement pattern. Based upon the previously discussed band assignments, the dominant low-energy transition of **1** is of different origin than the dominant low-energy transition observed in **2**. As such, a different resonance Raman enhancement pattern is expected and observed. The $S_{\pi}^{+} \rightarrow d_{z2}$ LMCT transition is expected to display stronger resonance enhancement of M-S modes, due to the increased M-S bonding character in the HOMO relative to the SOMO. Theoretical resonance Raman calculations for **2** (Figure 8B) are in excellent agreement with experiment, and full normal mode descriptions for the observed vibrations are given in Table 3. A particularly important mode includes the low energy dithiolene fold (experimental: 71 cm^{-1}, calculated: 52 cm^{-1}), and is central to the role that dithiolene bending plays in modulating metal-sulfur covalency through a pseudo Jahn-Teller effect (*vide infra*).

In order to understand the electronic structure changes of **2** relative to **1**, it is instructive to compare their resonance Raman spectra. Inspection of the two spectra (see Figure S-3 for an overlay) reveals that only a few of the vibrational modes observed for **2** appear to be resonantly enhanced in **1**. In particular, the Cp-M-Cp stretch is heavily mixed with the dithiolene fold in **2**. In fact, several C-S/M-S stretch and S-M-S bending modes are resonantly enhanced in **2**, and these directly probe the changes in M-L covalency that occur with the change in d-electron count, whereas these stretches are not observed in the resonance Raman spectrum of **1**. The fact that these modes are enhanced for **2** and not in **1** suggests that the degree of electron occupation in the d_{z2} orbital has strong effects on the nature of the M-L bonding. Multiple M-Cp vibrational modes are still present, but they are all mixed with M-S/C-S stretches or the dithiolene folding mode. Interestingly, the calculations show that several of the observed modes are combination and overtone bands (Table 3). For completeness, rR profiles of these bands are given in the SI (Figure S5). The rR profiles show that the transition responsible for band II involves a redistribution of electron density that is analogous to that observed in the ionization process of **1**, with a large change in the electron density of the bdt ligand.

The MIME effect in $Cp_2V(bdt)$. The MIME formalism can be used to show how the resonantly enhanced vibrations observed in the Raman spectrum of **2** (Figure 8B, 780 nm excitation) can be used to understand the nature of the vibrational modes that are activated during the **1** → $\mathbf{1}^+$ + e- photoionization process. We collected the rR spectrum of **2** on resonance with the $S_{\pi}^{+} \rightarrow d_{z2}$ LMCT transition, which results in a redistribution of electron density between these two orbitals. This LMCT electron density redistribution results in an excited state distortion for **2** that is very similar to the molecular distortion that occurs in the UPS of **1** *following photoionization of an $S_{\pi+}$ electron*. Fitting of the experimental rR spectrum[32] of **2** gives a set of excited state displacements (Table S-2) that can be used in combination with Equation 3 to determine the effective frequency associated with that observed in the UPS spectrum

of **1**. The iterative solution of Equation 3 using the parameters determined from the rR spectrum of **2** results in an effective frequency, ω_{eff} = 323 cm^{-1}, which is in good agreement with the vibronic progression frequency 383 cm^{-1} observed in the UPS data for **1**, particularly when considering that 1) compounds **1** and **2** contain metals with different d-electron counts, and 2) the rR spectrum is probing an *optical excitation*, while UPS is probing a UV photoemission. This MIME analysis for **2** demonstrates the power of rR spectroscopy, when used in conjunction with UPS, to develop a deep understanding of potential energy surfaces and excited state distortions that accompany photoexcitation.

The PJT effect in Cp$_2$V(bdt). The electronic driving force behind the dithiolene fold can now be understood within the context of a pseudo-Jahn-Teller (PJT) mechanism.[52-53] Briefly, a PJT effect arises from the vibronic coupling of the ground electronic state with one or more excited electronic states:

$$F_{0i} = \left\langle \Psi_0 \left| \frac{\delta V}{\delta Q_\Gamma} \right| \Psi_i \right\rangle \qquad (4)$$

PJT enables symmetry-forbidden mixing of states via a configuration interaction mechanism. Thus, the PJT mechanism provides a way for orthogonal orbitals (i.e. those that belong to different irreducible representations) in the high symmetry geometry to mix when the overall point symmetry is lowered. In order for a PJT effect to be observed, the triple product $\Gamma_0 \times \Gamma_Q \times \Gamma_i$ must contain the totally symmetric representation for at least one state Ψ_i. A simple two state, one mode vibronic Hamiltonian can be diagonalized to give an expression for the PJT adiabatic potential energy surfaces (APES) with surface energies $\varepsilon_\pm$ relative to the unperturbed states:

$$\varepsilon_\pm = \frac{1}{2} K_0 Q^2 \pm \sqrt{\Delta^2 + F^2 Q^2} \qquad (5)$$

where K_0 is the primary (non-vibronic) force constant, Δ is ½ of the energy gap between the mixing states,

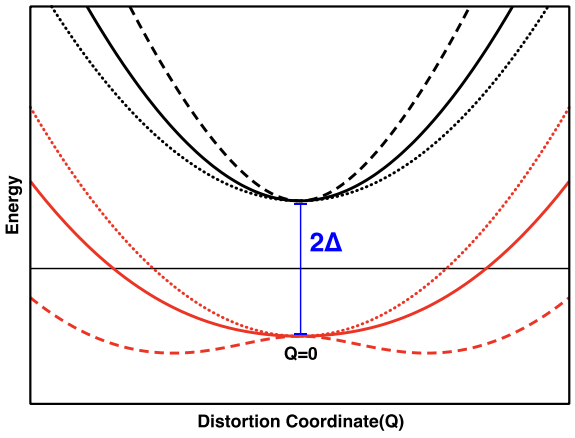

Figure 9: Depiction of upper (black) and lower (red) potential energy surfaces associated with varying values of F^2 (Eqn. 5). Dotted: $F^2 = 0$, solid: $F^2 = \Delta \cdot K_0$, dashed: $F^2 = 2\Delta \cdot K_0$. Note that when the critical condition $F^2 > \Delta \cdot K_0$ is met, the single-well ground state potential energy surface inverts into a double-well potential. This is the signature description of a *strong* PJT effect.

and Q is a dimensionless normal mode coordinate. At a certain threshold, ($F^2 > \Delta \cdot K_0$), the molecule becomes unstable with respect to a distortion along Q. This will result in a lowering of the symmetry from *effective* C_{2v} *to* C_s (Figure 9). From this equation, we can see that the three parameters which contribute to a large PJT distortion are a) small Δ, b) small K_0, and c) large F. These systems all contain a relatively large Δ term since the charge transfer excited states lie in the visible. Therefore, a low-frequency distorting mode (small K_0) is required in order to satisfy the above inequality for F^2. Thus, the low-frequency dithiolene folding mode enables the PJT effect in these molecules.

Crystal structures of **1-3** show a trend towards larger dithiolene fold with a decrease in d-electron count, which has been typically described in the context of increased metal ligand covalency in the redox orbital.[18] Here we will show how this can be more rigorously described within the context of a PJT active system that is tuned by a) LMCT energy, and b) the value of *F* to give a system capable of changing the magnitude of the PJT stabilization by nearly 20-fold.

For transitions that are well described by a single one-electron promotion, equation 3 can be rewritten in an orbital form:

$$F_{0i} = \left\langle \Psi_0 \left| \frac{\delta V}{\delta Q_\Gamma} \right| \Psi_i \right\rangle$$

$$= (q_a - q_b) \left\langle \phi_a \left| \frac{\delta V}{\delta Q_\Gamma} \right| \phi_b \right\rangle \quad (6)$$

$$= (q_a - q_b) f$$

where ϕ_a and ϕ_b are the donor and acceptor orbitals involved in the electronic transition and q_a and q_b are their respective occupation numbers (0,1, or 2). The quantity $q_a - q_b$ is equal to zero for $Cp_2Mo(bdt)$ (**1**), since both the S_π^+ and d_{z2} orbitals are filled. Thus, no folding distortion is observed in **1** since there is no driving force for a PJT effect. Compound **1** therefore provides a convenient benchmark for the non-vibronic force constant K_0, which is calculated to be only 2.8×10^{-3} mDyne/Å (corresponding to a 28

cm^{-1} mode). This small non-vibronic force constant is a necessary component (*vide supra*) for a large vibronic distortion. For $Cp_2Ti(bdt)$ (**3**), the acceptor orbital in the LMCT is unoccupied, and $q_b = 0$. The existence of a small non-vibronic force constant coupled with $q_a - q_b = 2$ for **3** leads to a large PJT effect with a concomitantly large folding distortion (*vide infra*).

$Cp_2Ti(bdt)$

Electronic Structure and Spectroscopy of $Cp_2Ti(bdt)$. The electronic absorption spectrum of **3** (Figure 10A) shows absorption features that are largely blue shifted relative to **1** and **2**. Band I is an energetically isolated intense transition that we assign as a $S_{\pi}^{+} \rightarrow d_{z2}$ LMCT. The increased intensity of Band I relative to **2** is explained by the large increase in S_{π}^{+}/d_{z2} orbital mixing that is driven by an additional reduction in d-electron count. The resulting increase in the ligand chelate fold angle allows for an increase in the overlap between the donor and acceptor orbitals relative to **1** and **2**. The rR spectrum of **3** (Figure 12B) shows C-S and M-S modes being more strongly enhanced relative to M-Cp modes when compared to the resonantly enhanced vibrational modes of **1** and **2**. Mode descriptions are given in Table 4. TD-DFT calculations suggest that band II can be assigned as a $S_{\pi}^{+} \rightarrow d_{xy}$ based transition (Figure 11), although a $S_{\pi}^{-} \rightarrow d_{z2}$ assignment cannot be completely dismissed at this point. The $S_{\pi}^{+} \rightarrow d_{xy}$ assignment for this transition is analogous to that seen as the lowest energy

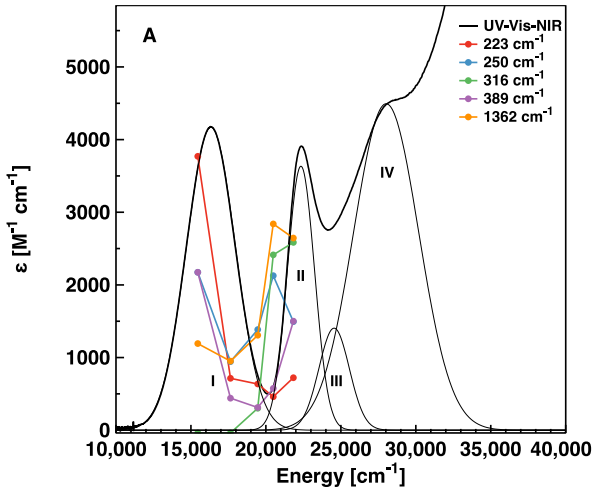

Figure 10A: Electronic absorption spectrum (CH_2Cl_2) and rR excitation profiles ($NaCl/Na_2SO_4$) of **3** (M=Ti). Gaussian resolved bands are denoted with roman numerals.

Figure 10B: Experimental ($NaCl/Na_2SO_4$) and theoretical (PBE0) resonance Raman spectra for **3**. Experimental excitation wavelength: 647 nm, theoretical: 500 nm (in resonance with calculated λ_{max}).

transition in **1**, but here it occurs at a higher energy due to the increased stabilization of the S_{π}^{+} orbital due to mixing with the d_{z2} orbital. The rR enhancement patterns with laser excitation in resonance with band II shows that the 321, 278, and 395 cm^{-1} modes are all strongly enhanced, with the 321 cm^{-1} mode being most enhanced. The calculated rR spectrum for band II (Figure S-4) shows that the strongest mode is at 299 cm^{-1} (calculated), and this mode corresponds to a M-Cp stretch, analogous to the 383 cm^{-1} mode observed in **1**. Interestingly, the observed resonance enhancement patterns for excitation into bands I and II are an example of orthogonal mode enhancement that arises from transitions that derive from completely different excitations. We can use this orthogonal resonance enhancement pattern to effectively rule out the $S_{\pi}^{-} \rightarrow d_{z2}$ assignment for band II, as this would be expected to possess a nearly identical rR profile as the $S_{\pi}^{+} \rightarrow d_{z2}$ transition responsible for band I. A complete listing of the TD-DFT computationally assisted band assignments is presented in Table S-3.

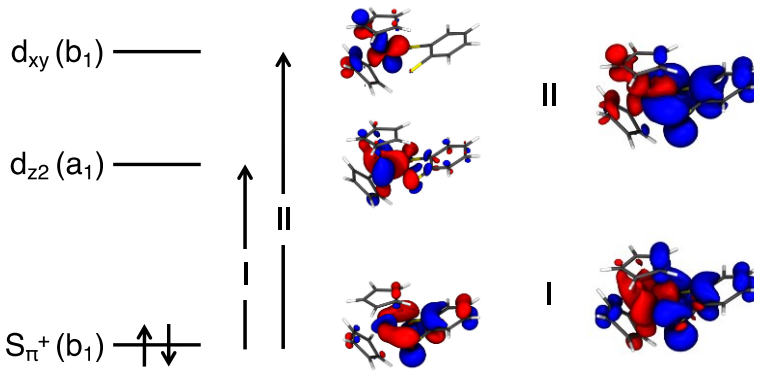

Figure 11: Frontier molecular orbitals for **3**. Arrows denote major transitions in the low-energy LMCT region. EDDMs for the transitions are given on the right (blue: electron loss, red: electron gain). Isovalues: 0.04 (orbitals), 0.004 (EDDM).

Of particular note is that the two most enhanced modes found in the calculated rR spectrum of **3** (Figure 10B) that are in resonance with band I involve some ditholene fold character. This can be understood within the context of the PJT potential energy surfaces for **3**, *vide infra*. The M-Cp modes are observed to be quite weak, demonstrating the minimal amount of d_{xy} population in the excited state (which is responsible for the large enhancement seen in **1)**. The M-S based distortions expected for a transition based on a one-electron promotion between highly mixed S_{π}^{+} and d_{z2} orbitals are dominant in the spectrum as compared to **1** in which the lowest energy absorption feature corresponds to a transition involving the strongly M-Cp anti-bonding d_{xy} orbital.

The PJT effect in $Cp_2Ti(bdt)$. Compound **3** is an example of a system that displays a strong PJT effect. DFT calculations on the *high symmetry C_{2v} structure* (**3b**) show a pseudo-degenerate HOMO ($S_{\pi+}$) and LUMO (d_{z2}) with an orbital splitting of only 0.17 eV. The electronic ground state of high-symmetry **3b** has A_1 symmetry, and the HOMO → LUMO one-electron promotion results in an excited state of B_1 symmetry, which cannot directly mix with the A_1 ground state by CI. Using group theoretical arguments (Figure 12), a vibrational mode of B_1 symmetry is necessary for mixing these two states by a PJT mechanism. In support of the PJT argument, frequency calculations on the high-symmetry ground state geometry of **3b** show a single negative frequency mode (-343 cm^{-1}) of B_1 symmetry, and this is described as a Ti-bdt bending (i.e. ligand folding) mode.

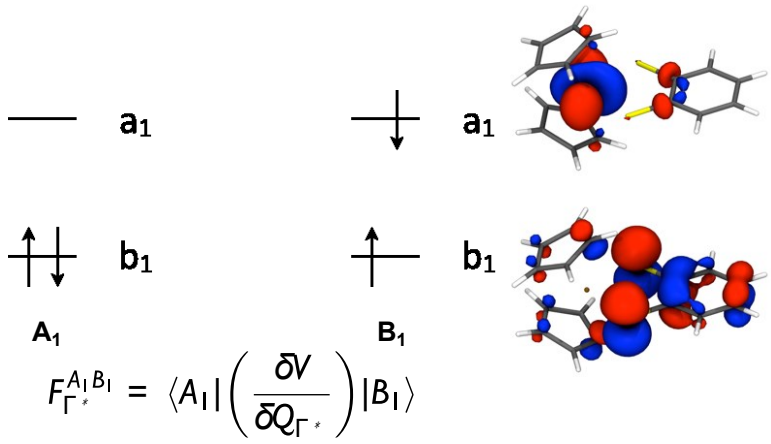

Figure 12: PJT mixing in $Cp_2Ti(bdt)$ of the B_1 excited state with the A_1 ground state results in a distortion and subsequent mixing of the metal and ligand orbitals. Isovalue: 0.04.

Using the orbital formalism that we developed above, we can quantitatively compare the nature of the PJT effect observed in **3** with that found for **2**, which is the d^1 analogue of **3**. By reducing the d-electron count from one in **2** to zero in **3**, we expect a 4-fold increase in F^2 for **3** from Eqn. 5. Note that this 4x increase is anticipated even in the absence of any differences in the donor and acceptor orbital character. However, using simple electronic repulsion arguments, the LMCT state energy splitting of **2** will be larger because its acceptor orbital is now singly occupied. DFT calculations on high symmetry unfolded **2** show that the HOMO/LUMO gap increases nearly 5-fold, to 0.80 eV. In addition, we see that the negative frequency at the point of instability ("unfolded" geometry) for **2** decreases in magnitude to -64 cm^{-1}. Using the second-order perturbation expression for the vibronic correction to the force constant, $K_v = -2F^2/\Delta$,[52-53] we note that this 5-fold increase in Δ combined with a 4-fold decrease in F^2 (from the occupation number change in Equation 5)

yields a remarkable 20-fold overall decrease in the vibronic contribution to the force constant. This flexible electronic structure is reflected in the sensitivity of the bdt → M charge-transfer state mixing with the electronic ground state as a function of the orbital occupation number (i.e. d-electron count, see Figure 9).

Conclusions

A complementary spectroscopic and theoretical study of model metal-dithiolene systems has been performed using a combination of electronic absorption, magnetic circular dichroism, resonance Raman, and gas-phase photoelectron spectroscopies. These data, coupled with the results of time-dependent DFT calculations, have been used to demonstrate how the very soft bending modes of the metal-dithiolene ring system are coupled to electronic structure. Specifically, the pseudo Jahn-Teller (PJT) effect provides an explanation for the low-symmetry distortions that are observed as a function of d-electron count in the $Cp_2M(bdt)$ (M=Ti, V, Mo) series of compounds. The electronic near-degeneracy of states in these high-symmetry complexes results in a strong distorting force along the metal-dithiolene fold angle leading to a strong dependence of the total energy with respect to the fold angle.[1] The PJT-induced mixing of LMCT states into the ground state is manifest by a large increase in metal-sulfur covalency that correlates with reduced d-electron count. The PJT effect is dramatically reduced as the d-electron count is increased, before being completely quenched in d^2 $Cp_2Mo(bdt)$. This study provides a theoretical foundation for understanding changes in Mo d-orbital electron count and metal-dithiolene folding as they pertain to the electronic structure of pyranopterin molybdenum enzymes, all of which possess at least one dithiolene chelate.

Several key points have emerged from this study that relate to the importance of the metal-dithiolene moiety in biological systems: 1) Distortions along the low energy dithiolene folding mode result in molecular bistability to yield a double potential well in the d^0 case (M=Ti here, or Mo/W(VI) in pyranopter-

in Mo and W enzyme families), with the minima corresponding to a "fold-up" and "fold-down" geometric configuration; 2) The nature of this potential energy surface arises from the strong PJT interaction between the ground state and a specific LMCT excited state (Figure 12) that are admixed by the resulting ligand fold distortion; 3) As the metal center d-electron count increases, the reduced PJT effect results in a softening and eventual elimination of the double-well potential. For the $Cp_2M(bdt)$ (M=Ti, V, Mo) systems discussed here, a single soft potential centered at $Q = 0$ predominates in the d^2 configuration. An analogous soft potential energy surface in the enzymes would allow for the sampling a wide range of Q with a low energetic penalty for the accompanying distortion. This PJT process provides the enzymes with a low energy pathway to minimize the reorganizational energy associated with changes in oxidation state[1] by coupling the mechanical motion of the pterin framework with overall oxidation state changes of the metal and the dithiolene. Thus, the effects of vibronic coupling that derive from redox active orbital occupancy may play a significant role in modulating the reduction potentials and catalytic reactivity of pterin containing Mo enzymes (Figure 1).

Finally, we have used resonance Raman spectroscopy to probe the important vibrational modes associated with electron reorganization among the S_π, d_{z2}, and d_{xy} orbitals. TD-DFT calculations were used to great effect in deconvoluting the experimental spectrum, and this enabled a description of the vibrations activated during the optical transitions and how these transitions differ due to orbital occupancy changes and PJT driven orbital mixing. From an intriguing merging of UPS and resonance Raman spectroscopy, the vibrational progression observed in the UPS spectrum of **1** has been understood in the context of the resonance Raman enhancement observed for **2**, which is a different molecule. Thus, the nature of the charge transfer transitions observed in **2** provides unique insight into the electron redistribution and molecular distortion found in the ionization/relaxation process of **1**. The combination of activated modes results in a “missing mode” often seen in vibrational progressions of optical spectra, but rarely described in an ionization process, as seen here.

AUTHOR INFORMATION

Corresponding Author

* (Word Style "FA_Corresponding_Author_Footnote"). Give contact information for the author(s) to whom correspondence should be addressed.

Present Addresses

†If an author's address is different than the one given in the affiliation line, this information may be included here.

Author Contributions

The manuscript was written through contributions of all authors. / All authors have given approval to the final version of the manuscript. / ‡These authors contributed equally. (match statement to author names with a symbol)

Funding Sources

Any funds used to support the research of the manuscript should be placed here (per journal style).

Notes

Any additional relevant notes should be placed here.

ACKNOWLEDGMENT

B. W. S. gratefully acknowledges the Los Alamos National Laboratory Glenn T. Seaborg Institute for a postdoctoral fellowship. M. L. K. would like to acknowledge the National Institutes of Health (GM-057378) for generous and continued financial support of our work on molybdoenzymes. J. H. E. thanks the National Institutes of Health (GM-037773) for support of portions of this work. D. L. L. (CHE-1664745) and M. L. K. (CHE 1565930) thank the National Science Foundation for their support.

ABBREVIATIONS

bdt, benzenedithiolate; Cp, cyclopentadienyl; DOMO, doubly occupied MO; LMCT, ligand-to-metal charge transfer; LUMO, lowest unoccupied molecular orbital; MCD, magnetic circular dichroism; MIME, missing mode effect; PJT, pseudo Jahn-Teller; rR, resonance Raman; PES, potential energy surface; SOMO, singly-occupied MO; (TD-)DFT, (time-dependent) density functional theory; QRO, quasi-restricted orbital; UPS, ultraviolet photoelectron spectroscopy.

REFERENCES

1. Cranswick, M. A.; Dawson, A.; Cooney, J. J. A.; Gruhn, N. E.; Lichtenberger, D. L.; Enemark, J. H., Photoelectron Spectroscopy and Electronic Structure Calculations of d^1 Vanadocene Compounds with Chelated Dithiolate Ligands: Implications for Pyranopterin Mo/W Enzymes. *Inorg. Chem.* **2007,** *46*, 10639-10646.
2. McCleverty, J. A., Metal 1,2-Dithiolene and Related Complexes. *Prog. Inorg. Chem.* **1968,** *10*, 49-221.
3. Stiefel, E. I., *Dithiolene Chemistry: Synthesis, Properties, and Applications*. John Wiley and Sons, Inc: Hoboken, New Jersey, 2003; Vol. 52.
4. Eisenberg, R.; Gray, H. B., Noninnocence in Metal Complexes: A Dithiolene Dawn. *Inorg. Chem.* **2011,** *50*, 9741-9751.
5. Cummings, S. D.; Eisenberg, R., Luminescence and Photochemistry of Metal Dithiolene Complexes. *Prog. Inorg. Chem.* **2003,** *52*, 315-367.
6. Kreickmann, T.; Hahn, F. E., Benzene-o-dithiolate ligands as versatile building blocks in supramolecular chemistry. *Chem. Commun.* **2007**, 1111-1120.

7. Faulmann, C.; Cassoux, P., Solid-State Properties (Electronic, Magnetic, Optical) of Dithiolene Complex-Based Compounds. *Prog. Inorg. Chem.* **2003,** *52*, 399-490.
8. Felton, G. A. N.; Vannucci, A. K.; Chen, J.; Lockett, L. T.; Okumura, N.; Petro, B. J.; Zakai, U. I.; Evans, D. H.; Glass, R. S.; Lichtenberger, D. L., Hydrogen Generation from Weak Acids: Electrochemical and Computational Studies of a Diiron Hydrogenase Mimic. *J. Am. Chem. Soc.* **2007,** *129* (41), 12521-12530.
9. Hissler, M.; McGarrah, J. E.; Connick, W. B.; Geiger, D. K.; Cummings, S. D.; Eisenberg, R., Platinum diimine complexes: towards a molecular photochemical device. *Coord. Chem. Rev.* **2000,** *208* (1), 115-137.
10. Hille, R., Structure and function of mononuclear molybdenum enzymes. *J. Biol. Inorg. Chem.* **1996,** *1*, 397-404.
11. Schindelin, H.; Kisker, C.; Rees, D. C., The molybdenum-cofactor: a crystallographic perspective. *Journal of Biological Inorganic Chemistry* **1997,** *2*, 773-781.
12. Li, H. K.; Temple, C.; Rajagopalan, K. V.; Schindelin, H., The 1.3 angstrom crystal structure of *Rhodobacter sphaeroides* dimethyl sulfoxide reductase reveals two distinct molybdenum coordination environments. *J. Am. Chem. Soc.* **2000,** *122* (32), 7673-7680.
13. Joshi, H. K.; Cooney, J. J. A.; Inscore, F. E.; Gruhn, N. E.; Lichtenberger, D. L.; Enemark, J. H., Investigation of metal-dithiolate fold angle effects: Implications for molybdenum and tungsten enzymes. *Proc. Natl. Acad. Sci. U.S.A.* **2003,** *100*, 3719-3724.
14. Rebelo, J. M.; Dias, J. M.; Huber, R.; Moura, J. J. G.; Romao, M. J., Structure refinement of the aldehyde oxidoreductase from *Desulfovibrio gigas* (MOP) at 1.28 angstrom. *J. Biol. Inorg. Chem.* **2001,** *6*, 791-800.
15. Kisker, C.; Schindelin, H.; Rees, D. C., Molybdenum-cofactor-containing enzymes: structure and mechanism. *Annu. Rev. Biochem* **1997,** *66* (1), 233-267.
16. Enroth, C.; Eger, B. T.; Okamoto, K.; Nishino, T.; Nishino, T.; Pai, E. F., Crystal structures of bovine milk xanthine dehydrogenase and xanthine oxidase: Structure-based mechanism of conversion. *Proc. Natl. Acad. Sci. U. S. A.* **2000,** *97*, 10723-10728.
17. George, G. N.; Pickering, I. J.; Pushie, M. J.; Nienaber, K.; Hackett, M. J.; Ascone, I.; Hedman, B.; Hodgson, K. O.; Aitken, J. B.; Levina, A.; Glover, C.; Lay, P. A., X-ray-induced photo-chemistry and X-ray absorption spectroscopy of biological samples. *J. Synchrotron Radiat.* **2012,** *19* (6), 875-886.
18. Lauher, J. W.; Hoffmann, R., Structure and Chemistry of Bis(Cyclopentadienyl)-ML_n Complexes. *J. Am. Chem. Soc.* **1976,** *98*, 1729-1742.
19. Fourmigue, M., Mixed cyclopentadienyl/dithiolene complexes. *Coord. Chem. Rev.* **1998,** *180*, 823-864.
20. Wiebelhaus, N. J.; Cranswick, M. A.; Klein, E. L.; Lockett, L. T.; Lichtenberger, D. L.; Enemark, J. H., Metal-Sulfur Valence Orbital Interaction Energies in Metal-Dithiolene Complexes: Determination of Charge and Overlap Interaction Energies by Comparison of Core and Valence Ionization Energy Shifts. *Inorg. Chem.* **2011,** *50* (21), 11021-11031.
21. Cooney, J. J. A.; Cranswick, M. A.; Gruhn, N. E.; Joshi, H. K.; Enemark, J. H., Electronic structure of bent titanocene complexes with chelated dithiolate ligands. *Inorg. Chem.* **2004,** *43*, 8110-8118.
22. Westcott, B. L.; Gruhn, N. E.; Enemark, J. H., Evaluation of molybdenum-sulfur interactions in molybdoenzyme model complexes by gas-phase photoelectron spectroscopy. The "electronic buffer" effect. *J. Am. Chem. Soc.* **1998,** *120*, 3382-3386.
23. Inscore, F. E.; McNaughton, R.; Westcott, B. L.; Helton, M. E.; Jones, R.; Dhawan, I. K.; Enemark, J. H.; Kirk, M. L., Spectroscopic evidence for a unique bonding interaction in oxo-molybdenum dithiolate complexes: Implications for sigma electron transfer pathways in the pyranopterin dithiolate centers of enzymes. *Inorg. Chem.* **1999,** *38* (7), 1401-1410.
24. Stephan, D. W., Sulfur-hydrogen and sulfur-sulfur oxidative addition to low-valent vanadium: synthesis and structure of monocyclopentadienyl- and dicyclopentadienylvanadium dithiolate derivatives. *Inorg. Chem.* **1992,** *31*, 4218-4223.
25. Kutoglu, A.; Kopf, H., Metallocene-Dithiol Chelates - Structural Elucidation and Synthesis of Benzene-1,2-Dithiolato-di(π-Cyclopentadienyl)-Molybdane(IV). *J. Organomet. Chem.* **1970,** *25*, 455-460.
26. Kopf, H.; Schmidt, M., Uber Einige π-Komplexstabilisierte Titan-Schwefel-Hetero-Cyclen. *J. Organomet. Chem.* **1965,** *4*, 426-429.
27. Lichtenberger, D. L.; Kellogg, G. E.; Kristofzski, J. G.; Page, D.; Turner, S.; Klinger, G.; Lorenzen, J., Inexpensive and high-precision digital power supply and counting interface for UPS, XPS, and Auger spectrometers. *J. Rev. Sci. Instrum.* **1986,** *57*, 2366.
28. Stoll, S.; Schweiger, A., EasySpin, a comprehensive software package for spectral simulation and analysis in EPR. *J. Magn. Reson.* **2006,** *178* (1), 42-55.
29. Humphrey, W.; Dalke, A.; Schulten, K., VMD: Visual Molecular Dynamics. *Journal of Molecular Graphics* **1996,** *14*, 33-38.
30. Neese, F., The ORCA program system. *Wiley Interdisciplinary Reviews: Computational Molecular Science* **2012,** *2* (1), 73-78.
31. Neese, F., Prediction of molecular properties and molecular spectroscopy with density functional theory: From fundamental theory to exchange-coupling. *Coord. Chem. Rev.* **2009,** *253* (5-6), 526-563.

32. Petrenko, T.; Neese, F., Analysis and prediction of absorption band shapes, fluorescence band shapes, resonance Raman intensities, and excitation profiles using the time-dependent theory of electronic spectroscopy. *J. Chem. Phys.* **2007,** *127*, 164319.
33. Neese, F.; Petrenko, T.; Ganyushin, D.; Olbrich, G., Advanced aspects of ab initio theoretical optical spectroscopy of transition metal complexes: Multiplets, spin-orbit coupling and resonance Raman intensities. *Coord. Chem. Rev.* **2007,** *251* (3-4), 288-327.
34. Weigend, F.; Ahlrichs, R., Balanced basis sets of split valence, triple zeta valence and quadruple zeta valence quality for H to Rn: Design and assessment of accuracy. *PCCP* **2005,** *7*, 3297-3305.
35. Perdew, J. P.; Burke, K.; Ernzerhof, M., Generalized Gradient Approximation Made Simple. *Phys. Rev. Lett.* **1996,** *77* (18), 3865-3868.
36. Petrenko, T.; Kossmann, S.; Neese, F., Efficient time-dependent density functional theory approximations for hybrid density functionals: Analytical gradients and parallelization. *Chem. Phys.* **2011,** *134* (5), 4116.
37. Adamo, C.; Barone, V., Inexpensive and accurate predictions of optical excitations in transition-metal complexes: the TDDFT/PBE0 route. *Theor. Chim. Acta* **2000,** *105* (2), 169-172.
38. Adamo, C.; Barone, V., Toward reliable density functional methods without adjustable parameters: The PBE0 model. *J. Chem. Phys.* **1999,** *110* (13), 6158-6170.
39. Neese, F.; Wennmohs, F.; Hansen, A.; Becker, U., Efficient, approximate and parallel Hartree-Fock and hybrid DFT calculations. A 'chain-of-spheres' algorithm for the Hartree-Fock exchange. *Chemical Physics* **2009,** *356* (1-3), 98-109.
40. Velde, G. T.; Bickelhaupt, F. M.; Baerends, E. J.; Guerra, C. F.; Van Gisbergen, S. J. A.; Snijders, J. G.; Ziegler, T., Chemistry with ADF. *J. Comput. Chem.* **2001,** *22* (9), 931-967.
41. Seth, M.; Ziegler, T.; Autschbach, J., Application of magnetically perturbed time-dependent density functional theory to magnetic circular dichroism. III. Temperature-dependent magnetic circular dichroism induced by spin-orbit coupling. *J. Chem. Phys.* **2008,** *129* (10), 104105.
42. Neese, F., Importance of Direct Spin−Spin Coupling and Spin-Flip Excitations for the Zero-Field Splittings of Transition Metal Complexes: A Case Study. *J. Am. Chem. Soc.* **2006,** *128* (31), 10213-10222.
43. Lichtenberger, D. L.; Gruhn, N. E.; Rai-Chaudhuri, A.; Renshaw, S. K.; Gladysz, J. A.; Jiao, H.; Seyler, J.; Igau, A., Vibrational Progressions in the Valence Ionizations of Transition Metal Hydrides: Evaluation of Metal-Hydride Bonding and Vibrations in (η^5-C_5R_5)Re(NO)(CO)H [R = H, CH_3]. *J. Am. Chem. Soc.* **2002,** *124*, 1417-1423.
44. Amashukeli, X.; Winkler, J. R.; Gray, H. B.; Gruhn, N. E.; Lichtenberger, D. L., Electron-transfer reorganization energies of isolated organic molecules. *J. Phys. Chem. A* **2002,** *106* (33), 7593-7598.
45. Amashukeli, X.; Gruhn, N. E.; Lichtenberger, D. L.; Winkler, J. R.; Gray, H. B., Inner-sphere electron-transfer reorganization energies of zinc porphyrins. *J. Am. Chem. Soc.* **2004,** *126* (47), 15566-15571.
46. Gruhn, N. E.; da Silva Filho, D. A.; Bill, T. G.; Malagoli, M.; Coropceanu, V.; Kahn, A.; Bredas, J.-L., The Vibrational Reorganization Energy in Pentacene: Molecular Influences on Charge Transport. *J. Am. Chem. Soc.* **2002,** *124*, 7918-7919.
47. Closs, G. L.; Miller, J. R., Intramolecular Long-Distance Electron-Transfer in Organic-Molecules. *Science* **1988,** *240*, 440-447.
48. Tutt, L. W.; Zink, J. I.; Heller, E. J., Simplifying the MIME: a formula relating normal mode distortions and frequencies to the MIME frequency. *Inorg. Chem.* **1987,** *26* (13), 2158-2160.
49. Solomon, E. I., Inorganic Spectroscopy, An Overview. In *Comments Inorg. Chem.*, Sutin, N., Ed. Gordon and Breach: New York, 1984; Vol. 3, pp 225-320.
50. Avoird, A.; Ros, P., *Theoretica Chimica Acta* **1966,** *4*, 13-21.
51. Solomon, E. I.; Szilagyi, R. K.; DeBeer George, S.; Basumallick, L., Electronic Structures of Metal Sites in Proteins and Models: Contributions to Function in Blue Copper Proteins. *Chemical Reviews* **2004,** *104*, 419-458.
52. Bersuker, I. B., *Electronic structure and properties of transition metal compounds: introduction to the theory*. 2nd ed.; Wiley: Hoboken, N.J., 2010; p 759.
53. Bersuker, I. B., Modern aspects of the Jahn-Teller effect theory and applications to molecular problems. *Chemical Reviews*
2001, *101* (4), 1067-114.

Table 1: $Cp_2Mo(bdt)$ vibrational modes.

Exp.	Exp. Int.	Calc.	Calc. Int.	Mode description
Not obs.		28	0.04	Dithiolene fold
236	0.20	274	0.20	M-Cp str. (s) + C-S ip bend
286	0.61	330	0.47	M-Cp str. (as) + C-S ip bend
383	1	390	1	Cp-M-Cp str. (s)
593	0.34	584	0.21	M-Cp str. (single Cp)
1098	0.25	1084	0.20	C-S str. + C-C str.
1438	0.29	1430	0.11	Ph ring mode
Raman excitation wavelengths: Exp. 488 nm, Calc. 444 nm.				

Table 2: Normal mode displacements and Huang-Rhys factors for the $Cp_2Mo(bdt)$ ionization from TD-DFT calculations.

Mode (cm^{-1})	$\lvert\Delta\rvert$[a]	S[b]	Description
311	1.9	1.9	Cp-M stretch
332	2.5	3.0	Cp-M stretch
474	6.8	23	C-S/M-S stretch

[a]Dimensionless. $\Delta = \sqrt{\frac{\omega}{\hbar}}\boldsymbol{LqM}^{\frac{1}{2}}$, where M are the atomic masses, q are the cartesian displacements, and L are the normal modes. [b]$S = \Delta^2/2$.

Table 3: $Cp_2V(bdt)$ vibrational modes.

Exp.	Exp. Int.	Calc.	Calc. Int.	Mode description
71	0.79	52	0.47	Dithiolene fold
266	1	249	1	M-Cp str. (s) + dt fold
319	0.32	300	0.17	52 + 249 combination
		304	0.19	M-Cp str. (s) + S-M-S ip bend
478	0.61	470	0.46	C-S str. (s) + ring str.
526	0.12	497	0.18	249 overtone
735	0.09	719	0.17	249 + 470 combination
828	0.16	794	0.14	?
833	0.12	802	0.20	?
1092	0.79	1077	0.48	C-S + C-C str.
1432	0.40	1418	0.21	Ph ring mode
Raman excitation wavelengths: Experimental: 780 nm, Theoretical: 855 nm.				

Table 4: $Cp_2Ti(bdt)$ vibrational modes.

Exp.	Exp. Int.	Calc.	Calc. Int.	Mode description
Not obs.	-	57	0.99	Dithiolene fold
157	0.70	151	0.47	M-S Stretch
178	0.87	171	0.29	M-Cp str. + dt fold
223	0.94	209	0.75	S-M-S bend + M-S str.
255	0.8	250	0.55	M-Cp str + dt fold
270	0.54	254	1.0	Dithiolene fold + M-Cp str (as)

316	0.29	307	0.12	57 + 250 combination
325	0.26	312	0.22	57 + 254 combination
389	0.66	378	0.51	M-S str.
471	1.0	470	0.90	C-S str. + Ph ring mode
Raman excitation wavelengths: Experimental: 647 nm, Calculated: 526 nm.				